Mechanics of low-angle extensional shear zones at the brittle-ductile transition

F. Gueydan, Y. Leroy, Laurent Jolivet

Mechanics of low-angle extensional shear zones at the brittle-ductile transition

Frédéric Gueydan
Géosciences Rennes, UMR CNRS 6118, Université Rennes 1, Rennes, France

Yves M. Leroy
Laboratoire de Mécanique des Solides, UMR CNRS 7649, Ecole Polytechnique, Palaiseau, France

Laurent Jolivet
Laboratoire de Tectonique, UMR CNRS 7072, Université Pierre et Marie Curie, Paris, France

Received 18 September 2003; revised 7 July 2004; accepted 17 September 2004; published 30 December 2004.

[1] Low-angle midcrustal ductile shear zones and the related microseismic activity recorded below regions of active extension are seen here as two consequences of strain localization. The feldspar-to-mica reaction which occurs once feldspar grains are fractured is the destabilizing mechanism selected to explain the strain localization. The model problem considered to substantiate these claims is solved by numerical means and combines the simple shear due to the rigid gliding of the upper crust (at the velocity of V_s) and the stretch resulting from the extension of the whole crust (at the velocity V_e). The rheological model accounts for dislocation creep of quartz, feldspar, and mica, the feldspar-to-mica reaction, and its prerequisite, which is the feldspar fracturing detected by the Mohr-Coulomb criterion. The one-dimensional (1-D) solution, which constrains shear bands to be horizontal, shows the depth partitioning in deformation mode between the simple shear of the low-viscosity deep crust and the stretching of the highly viscous midcrust. Strain localization occurs during rapid increase of the shearing velocity V_s, corresponding to low values of the velocity ratio V_e/V_s. The 2-D solution (for $V_e/V_s = 10^{-3}$) reveals the development of a periodic system of extensional shear bands, dipping at 30° toward the shearing direction at a depth of 12 to 14 km. Shear bands are formed after less than half a million years at the base of the reaction zone defined by the region where feldspar-to-mica reaction is completed. Shear bands do not propagate to greater depths because the pressure prevents the feldspar from fracturing and thus the reaction to occur. The periodic system of shear bands defines a midcrustal flat weakened zone within which the equivalent shear stress is enhanced by at least a factor of three at the shear band tips. Brittle fracture could thus occur within the midcrustal flat weakened zone, explaining therefore the microseismicity monitored at these depths in regions of active extension. *INDEX TERMS:* 8109 Tectonophysics: Continental tectonics—extensional (0905); 8159 Tectonophysics: Rheology—crust and lithosphere; 8164 Tectonophysics: Stresses—crust and lithosphere; 7218 Seismology: Lithosphere and upper mantle; 3230 Mathematical Geophysics: Numerical solutions; *KEYWORDS:* continental extension, strain localization, detachment fault, rheology, reaction softening, numerical model

Citation: Gueydan, F., Y. M. Leroy, and L. Jolivet (2004), Mechanics of low-angle extensional shear zones at the brittle-ductile transition, *J. Geophys. Res.*, *109*, B12407, doi:10.1029/2003JB002806.

1. Introduction

[2] The two objectives of this paper are first to study the origin of low-angle extensional shear zones at the brittle ductile transition of the extending continental crust and, second, to reconcile, tentatively, the apparent contradiction between their observed subhorizontal orientation with the approximately ±45° predicted by classical failure criteria for frictionless materials.

[3] Low-angle faults and shear zones are typical of core-complexes in an extensional, postorogenic phase. Regional studies have indeed shown with little ambiguity that normal faulting can occur with a low original dip, defining a brittle detachment, as in the Basin and Range province [*Wernicke*, 1981; *Burchfiel et al.*, 1987; *Lister and Davis*, 1989], the Woodlark Basin [*Abers*, 1991; *Abers et al.*, 1997] or the Aegean region [*Lister et al.*, 1984; *King et al.*, 1985; *Avigad et al.*, 1998]. Flat-lying brittle detachment and brittle-ductile extensional shear zones with such low dip cannot be explained from the expected material strength and stress state [*Jackson*, 1987; *Wernicke*, 1992, 1995] using classical

0148-0227/04/2003JB002806$09.00

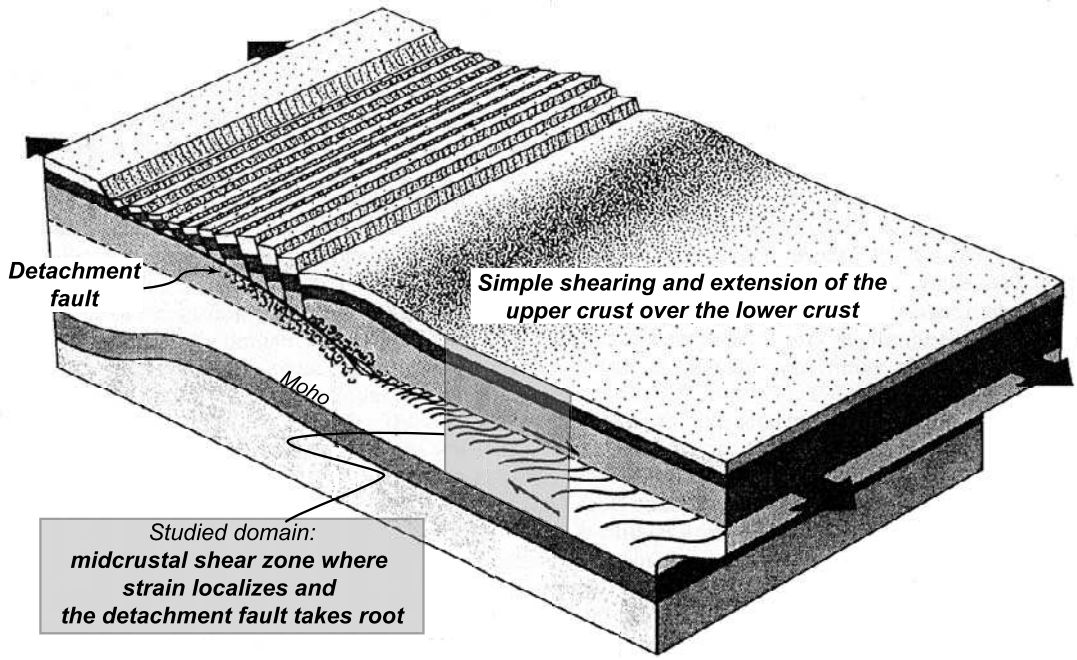

Figure 1. Schematic drawing of a metamorphic core complex showing the relation between detachment fault and extensional shear zone [after *Lister and Davis*, 1989].

Andersonian mechanics [*Anderson*, 1951] and question the overall mechanical behavior of the continental crust.

[4] The subhorizontal orientation of faults in the upper crust, despite the extensional regime which should promote failure with a dip of 45 to 60° in a pristine frictional formation, has been much debated leading to two main ideas. The first idea is the rotation of the principal stress directions to create initial low-dip angle normal fault [*Melosh*, 1990]. The second idea is the flexural rotation of the hanging wall leading to the deactivation of the fault initiated with the expected high dip-angle [*Buck*, 1988; *Wernicke and Axen*, 1988]. The rotation of the principal stress directions at midcrustal depths is obtained with a crust sustaining a combined simple shear and extension [*Melosh*, 1990] but the linear viscosity model used for that construction, however, cannot explain the trend toward failure which is assumed in this paper to be initiated by strain localization. Moreover, the rotation of the principal stresses has to be accompanied by sufficient increase in deviatory stress to trigger low angle faulting, as discussed by *Abers* [2001]. To this end, *Westaway* [1999] proposed that, in the case of a rapid extension, a large strain-rate ductile flow takes place at the base of the brittle crust. Constraints on the temperature and rheological conditions which could justify this conjecture will not be elaborated further in this paper and we shall concentrate on the formation of low-angle extensional shear zone within the brittle-ductile transition where flat-lying brittle detachments are often rooted [*Lister and Davis*, 1989; *Gautier and Brun*, 1994] (Figure 1). The second idea often evoked is the flexural rotation of the hanging wall of the initially high-angle normal fault and is reminiscent of the classical book-shelf mechanism [*Mandl*, 1988]. The fault is thus initiated with the expected dip but, because of flexure of the ruptured upper-crust plate and isostatic compensation, is rotated and deactivated. A more favorably oriented fault is then initiated or activated and will subsequently sustain the same convection and, finally, deactivation. The low-angle fault which is now observed is the envelope of these series of faults which were, very likely, never simultaneously activated, as illustrated in Figure 1.

[5] The objective of this paper is not to elaborate further on those two ideas, despite the need for further field data confrontation, but to concentrate on a particular aspect of the envelope fault defined above and referred to as a detachment fault. Our interest is with the rooting of that fault in the upper part of the lower crust at the brittle-ductile transition (Figure 1). Because of the large distance between the rotated blocks of the brittle crust and the zone where the deformation is ductile and localizes, it is proposed here to set aside the questions raised by the brittle crust faulting and to concentrate our effort solely on the brittle-ductile transition. Linking the two structural processes is of course of great interest but is postponed to future work. At the brittle-ductile transition, it has been conjectured that the fault remains subhorizontal and its development guided by a shear zone in which strain localizes. The theoretical questions considered in this paper are first the justification, from the rheological point of view, why the ductile strain localizes at that specific depth and second, why the shear zone is so flat despite the definite amount of stretching at that depth.

[6] These shear zones form under P-T conditions of the greenschist facies, within or close to the brittle-ductile transition [*Miller et al.*, 1983; *Jolivet et al.*, 1998; *Jolivet and Patriat*, 1999]. Field evidence suggests that these shear

zones correspond to domains of high permeability, where fluids percolate, leading to the formation of numerous quartz-rich veins [e.g., *Patriat and Jolivet*, 1998]. These shear zones are also evidenced by seismic profiles and microseismicity recorded in active regions. In the northern Aegean Sea, seismic profiles show shallow dipping reflectors in the downward prolongation of major normal faults [*Laigle et al.*, 2000]. The shallow-dipping detachment of the southern margin of the Gulf of Corinth proposed by *Sorel* [2000] could root at depth in a seismically active décollement at the brittle-ductile transition [*Rietbrock et al.*, 1996; *Rigo et al.*, 1996]. The destabilizing factor responsible for strain localization at midcrustal depths and the low dip angle of these shear zones are two prerequisite questions to be considered before discussing the microseismicity, as it will be done in this paper.

[7] Within the lower ductile crust, shear heating [*Fleitout and Froidevaux*, 1980; *Ord and Hobbs*, 1989], grain size reduction [*Rutter and Brodie*, 1988; *de Bresser et al.*, 2001] and reaction-softening are the most common destabilizing factor responsible for strain localization. Shear heating and grain size reduction are temperature-sensitive mechanisms and more relevant for depths close to the Moho [*Poirier*, 1980; *Braun et al.*, 1999; *Gueydan et al.*, 2001]. At midcrustal depths, reaction-softening, due mostly to feldspar to mica reaction, remains thus the major destabilizing factor responsible for strain localization [*Mitra*, 1978; *White and Knipe*, 1978; *Dixon and Williams*, 1983; *Wibberley*, 1999]. This phase transformation required feldspar fracturing [*Simpson*, 1985; *Fitz Gerald and Stünitz*, 1993]. *Gueydan et al.* [2003] (referred to as paper 1 hereafter) have incorporated these features in a rheological model for a mixture of three phases, feldspar, quartz and mica, undergoing dislocation creep at a common strain rate. The 1-D simple shear analysis of the lower crust they proposed showed the formation of a horizontal shear zone at the brittle-ductile transition after less than half a million years. The depth of the shear zone is mostly governed by the Mohr-Coulomb criterion used to detect this fracturing and by the time lapse t_L during which the shearing velocity V_s is increased. The time required for the shear band to form depends on the reaction kinetics. Timing and depth were consistent with PT constraints obtained in the field for the East Tenda Shear Zone, Alpine Corsica, France.

[8] In paper 1, the kinematics of simple shear was proposed to explain horizontal shear zones disregarding the extension of the crust. In this paper, a component of extension is combined to the simple shear which remains however dominant, as suggested by geological observations. Metamorphic core complexes and detachments mostly form in postorogenic extensional context. In the Tyrrhenian and the Aegean Seas extensional shear zones at the brittle-ductile transition and major normal faults show a constant polarity on several hundreds of kilometers (top-to-the-east in the Tyrrhenian Sea, top-to-the-north in the Aegean Sea) suggesting a significant component of simple shear [*Jolivet et al.*, 1994, 1998].

[9] This paper presents a 2-D thermomechanical model of an extending crust based on the rheology defined in paper 1. The prototype of the extending continental crust is first presented and consists of ductile layers sustaining a flow which combines stretch and shear by applying appropriately the velocities V_e and V_s, respectively, at the boundaries. The 1-D finite-element solutions of this combined flow show a depth partitioning in deformation mode between the midcrust, mostly dominated by pure shear, and the deep crust, sustaining simple shearing. The velocity ratio V_e/V_s has to be as low as 10^{-3} for localization to take place at the depth of ~13 km which is the base of the reaction zone below which the feldspar-to-mica reaction is not activated. The 2-D finite-element solutions presented show the formation of a flat weakened zone at the brittle-ductile transition, defined by a periodic system of low dipping extensional shear zones. Finally, the stress state within the weakened zone is examined in details to shed light on potential microearthquakes and local fluids migration at that depth.

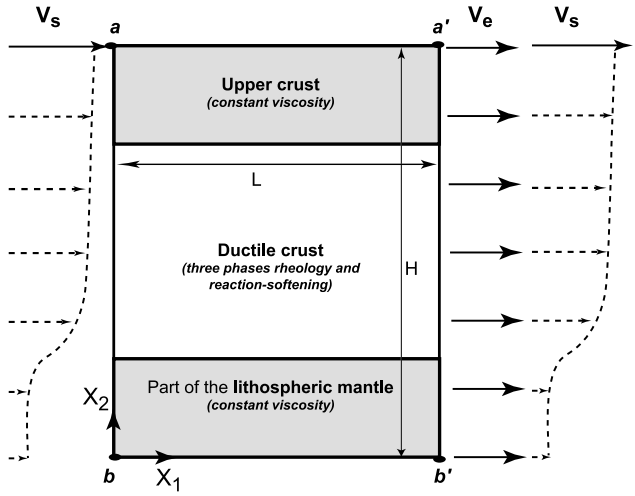

Figure 2. The prototype of the extending continental crust, with its periodic boundary conditions, corresponds to the shaded region in Figure 1.

2. Prototype of the Extending Continental Crust

[10] This section presents the prototype adopted for the continental crust including the constitutive relations which are the 3-D extension of the rheological model presented in paper 1.

2.1. Geometry, Boundary Conditions, and Numerical Scheme

[11] The upper crust is seen as a block sustaining an overall extension (at a velocity V_e) and gliding over the rest of the layered structure, at a velocity V_s, as it is schematically illustrated in Figure 2 and motivated in the introduction. The overall simplified kinematics is thus a combination of extension of the entire crust and simple shear. The changes in time of the shearing velocity V_s should be seen as a result of the remote and complex faulting in the upper crust, which again, is not described in that paper.

[12] The layered structure presented in Figure 2 has the total initial thickness H of 40 km and is composed of the upper and lower crusts and of the upper lithospheric mantle. The length L of the structure is set arbitrary to 20 km. The overall kinematics described above leads to

the following boundary conditions for the structure assumed periodic in the horizontal direction between the section ab and $a'b'$ (Figure 2). Any point along $a'b'$ has the velocity of the point at the same depth along ab plus the velocity V_e, corresponding to the overall stretching of the structure. The velocity at point a is further constrained by requiring its value to be V_s, to reproduce the overall gliding of the upper crust over the rest of the structure. This additional constraint is not imposed between other points along ab and $a'b'$ to leave sufficient freedom for the structure to develop a nonuniform simple shear superposed to the stretching mode. In summary, the periodic boundary conditions in terms of velocity impose that the ductile crust sustains a simple shear governed by V_s combined to an extension controlled by the velocity V_e.

[13] The time history of the prescribed velocities is as follows. The velocity V_e is initially zero so that the initial conditions correspond to a steady state in simple shear. The two velocities V_s and V_e are increased during a time interval t_L. The velocities are then kept constant thereafter. This time increase of the velocities is justified by the findings of paper 1 where destabilizing effects were triggered away from steady state conditions. Moreover, a condition for localization is that the final velocity, reached after the time t_L, is at least five times the initial velocity. This condition is explained by the necessity to raise the shear stress for triggering feldspar fracturing and thus for initiating the phase transformation. The steady state defining the initial conditions is characterized by a classical rheological layering that relies on further assumptions on the rheology of the upper crust and the upper mantle. Since our main interest is strain localization at midcrustal depths, the upper crust and the upper lithospheric mantle are assumed viscous (with a constant viscosity), for sake of simplicity.

[14] The 1-D and 2-D solutions of this thermomechanical boundary value problem are found by numerical means using the finite-element method implemented in the code SARPP [*Structural Analysis and Rock Physics Program*, 2003]. A Lagrangian description of the deformation is adopted and the incompressibility constraint imposed by penalty (coefficient of 2.4×10^7 MPa) so that the nodal unknowns are the displacement and the temperature. Note that the periodic boundary conditions are also enforced by penalty. The upper crust and the upper lithospheric mantle are discretized by two sets of 40×5 nine-noded Lagrangian elements for the 2-D analysis. The lower crust is partitioned into 40×30 elements of the same type. This discretization, as well as the element type selected, was found to be sufficient to capture strain localization. More precisely, 2-D results will be presented in a subregion of the structure which is discretized by 40×15 elements having an aspect ratio of 1.1. The heat equation is solved over the whole structure with radiogenic heat production and shear heating contribution in the ductile crust corresponding to the conversion of mechanical work into heat. The boundary conditions for the thermal problem are the flux from the mantle set to 30 mW/m^2, and the surface temperature kept to 300°K. Mechanical equilibrium and temperature evolution are solved in a staggered manner. Further information on the numerical scheme is given by *Gueydan* [2001].

2.2. Constitutive Relations Leading to Localization at the Brittle-Ductile Transition

[15] The layered structure presented above is composed of a material described as an incompressible non-Newtonian fluid such that the Kirchhoff stress tensor $\underline{\underline{\tau}}$ is given by

$$\underline{\underline{\tau}} = 2\eta(\dot{\varepsilon}, C_\alpha, p, T)\underline{\underline{D}} - p\underline{\underline{I}}, \tag{1}$$

where p, η and $\underline{\underline{D}}$ are the pressure, the secant viscosity and the rate of deformation tensor, respectively. The definition of the arguments of the viscosity will be given in this section. The material incompressibility constrains the trace of $\underline{\underline{D}}$ to be zero. Note that tensors and vectors are underlined twice and once, respectively. Equation (1) is the multidimensional generalization of the creep law

$$\tau = \eta(\dot{\varepsilon}, C_\alpha, p, T)\dot{\varepsilon}, \tag{2}$$

where the equivalent stress τ and strain rate $\dot{\varepsilon}$ are defined by

$$\tau = \sqrt{\frac{1}{2}\underline{\underline{\tau}} : \underline{\underline{\tau}}} \quad , \quad \dot{\varepsilon} = \sqrt{2\underline{\underline{D}} : \underline{\underline{D}}}. \tag{3}$$

The product: between two second-order tensors $\underline{\underline{A}}$ and $\underline{\underline{B}}$ results in the scalar $A_{ij}B_{ji}$ in a Cartesian coordinate system.

[16] The rheological model defined in (1) to (3) is also applied to the upper mantle and the upper crust with the restriction that the viscosity η is set to the constant value $10^{23} Pa.s$. This value is large, but of the same order as the viscosity that will be found in the upper part of the lower crust. In the lower crust, the proposed constitutive model, discussed at length in paper 1, is based on observations of an exhumed midcrustal shear zone, Tenda massif, Alpine Corsica, France. There, the amount of feldspar transformed into mica is found to increase with increasing shear strain. It is thus assumed that the Representative Elementary Volume, REV, is composed of three phases, feldspar, mica and quartz, in concentration C_α (with α set to f, m and q, respectively). The three phases deform at the same equivalent strain rate $\dot{\varepsilon}$ and the secant viscosity η defined in (2) is then the sum of the viscosity of each phase weighted by their concentration

$$\eta = C_f\eta_f + C_m\eta_m + C_q\eta_q, \tag{4}$$

with the condition $C_f + C_m + C_q = 1$ at any time.

[17] Each phase deforms by dislocation creep, a deformation mechanism which is temperature and strain rate sensitive and described by the following power-creep law

$$\dot{\varepsilon} = A_\alpha \exp\left(-\frac{Q_\alpha}{RT}\right)\tau_\alpha^{n_\alpha}, \tag{5}$$

in which τ_α, A_α, Q_α and n_α are the partial equivalent shear stress, the preexponential constant, the activation energy and the stress exponent, respectively. Values for the rheological parameters, as well as the initially uniform distribution of the phase concentration, are found in Table 1.

Table 1. Rheological Parameters for Dislocation Creep Based on Three Data Sets From *Shelton and Tullis* [1981], *Koch et al.* [1989], and *Kronenberg et al.* [1990] for Feldspar, Quartz, and Biotite, Respectively

Parameters	Feldspar	Quartz	Mica
Q, kJ mol^{-1}	238	134	51
n	3.2	2.7	18
A, MPa^{-n} s^{-1}	3.27 10^{-4}	1.16 10^{-7}	1. 10^{-30}
Initial C_α	0.4	0.5	0.1

The partial viscosities $\eta_\alpha = \tau_\alpha/\dot{\varepsilon}$ introduced in equation 4 are thus function of the common strain rate and the temperature.

[18] The essential ingredient of this rheological model is the gradual transformation of feldspar into mica which leads, as it will be shown, to a destabilizing factor responsible for strain localization. This transformation occurs according to the evolution law

$$\dot{C}_m = -\dot{C}_f = \delta\varphi\dot{\varepsilon}(C_m^* - C_m). \tag{6}$$

The rate of transformation is assumed to be proportional to the equivalent strain rate, to the dimensionless kinetics constant φ and to the difference in mica concentration between the present and the final concentration C_m^* found in the core of the localization zone (close to 0.5 in the Tenda Massif, Corsica). The feldspar-to-mica transformation only occurs if feldspar grains are first fractured. Grain fracturing takes place according to the Mohr-Coulomb criterion

$$\begin{aligned} &\text{Grain fracture } \eta_f\dot{\varepsilon} - \mu p \geq 0 \rightarrow \delta = 1, \\ &\text{No grain fracture } \eta_f\dot{\varepsilon} - \mu p < 0 \rightarrow \delta = 0, \end{aligned} \tag{7}$$

in terms of the partial equivalent stress $\eta_f\dot{\varepsilon}$ acting on the feldspar phase. This criterion sets the value of the scalar δ in the evolution law (6) at any time. Note that no memory is preserved of previous intrusion in the fracture domain: a decrease of the feldspar partial stress below the critical value defined by (7) sets δ to zero and stops the reaction defined in (6).

[19] The evolution in time of the mica concentration and of the secant viscosity η of the REV is sketched in Figure 3, assuming a constrain strain rate. The proportion of mica increases with time at a rate which is faster for larger values of φ, as it is illustrated with change in φ by a factor 10 in Figure 3a. This influence is due to the characteristic time $t_R = 1/\varphi\dot{\varepsilon}$ which is proportional to the initial rate of reaction, as can be see from equation (6). Increasing the strain rate or the kinetic constant by a factor of 10 decreases the time necessary for most of the phase reaction to take place. The initial protolith has a large secant viscosity, because of the small mica content, compared to the mylonite, since mica has the lowest viscosity (Figure 3b). The increase in mica concentration results in a drop in secant viscosity resulting in an overall softening of the REV, responsible for the strain localization. The reaction time t_R therefore partly controls the time during which strain localization can take place. Indeed, it has been shown in paper 1 that φ has to be greater than 10^3 for localization to occur within the lower crust sustaining simple shear.

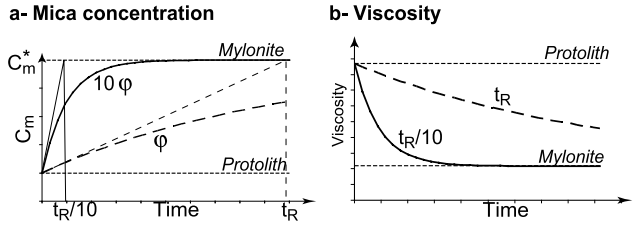

Figure 3. A schematic description of the evolution (a) of the mica phase concentration and (b) of the secant viscosity of the REV starting from the protolith and ending with the mylonite. This evolution is controlled by the kinetics of the feldspar-to-mica reaction (φ) and the strain rate ($\dot{\varepsilon}$) and requires feldspar fracturing. An increase of φ or of the strain rate by an order of magnitude significantly decreases the reaction time $t_R = 1/\varphi\dot{\varepsilon}$ and leads to faster drop in the REV viscosity.

[20] The first attempt in understanding the consequences of this rheological model consists in applying it to the lower crust assuming pure extension and results in the rheological envelope presented in Figure 4. The feldspar grains are fractured in the upper part of the lower crust according to the Mohr-Coulomb criterion. The transformation, once completed, results in a reaction zone which is weaker than the protolith. The reaction zone is thus the region where the feldspar-to-mica reaction is activated. Its lower boundary is the feldspar brittle-ductile transition. Strain localization should occur within the reaction zone during the protolith to mylonite transformation. The 1-D and 2-D numerical solutions presented in the next section will document this progressive transformation, the transient development of reaction zones, its geometry and internal structure.

[21] Before proceeding, it should be stressed that the rheological properties are obtained from laboratory creep tests (Table 1) except for the initial and final mica concentrations C_m^*, the kinetics constant φ and the friction coefficient μ for feldspar fracturing. The field data collected in the East-

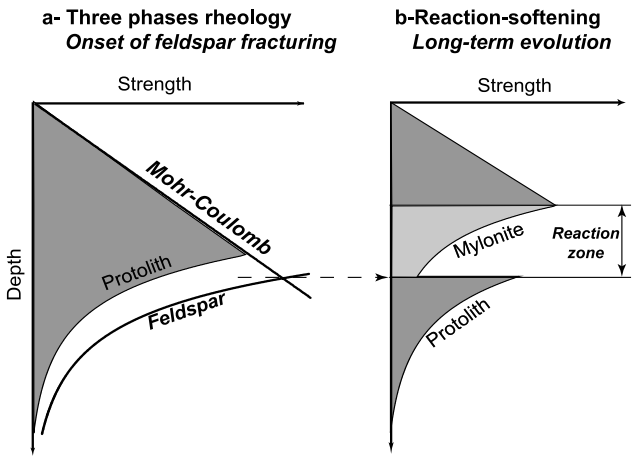

Figure 4. Rheological envelope of the continental crust. The initial continental strength is based on the protolith strength. The onset of feldspar fracturing (Figure 4a, MC line) is a prerequisite to the progressive transformation from protolith to mylonite in the reaction zone (Figure 4b).

Tenda Shear Zone provide the two concentrations. The simple shear analysis of paper 1 has revealed that the kinetics constant should be 10^5 and the friction coefficient 0.2 for the localization to be at the depth of 12 km and the shear zone to be kilometer thick. Those values are the one considered in this paper although a parametric study will be presented in the next section. It should be also mentioned that the dimensional analysis considered is identical to the one presented in paper 1 and is not repeated here for sake of brevity. Note that the characteristic time for conduction over the structure is 14 Ma providing the reference strain rate $\dot{\varepsilon}_R$ of $2.210^{-15}s^{-1}$. Note also that the reference velocity V_R, defined by $V_R = \dot{\varepsilon}_R/L$, is then 1.4 mm/a.

3. One-Dimensional Solution for Combined Shear and Extension

[22] The aim of this section is to select the relevant range of velocity ratios V_e/V_s for the 2-D problem based on the depth of the transformation zone and the rotation of the principal stress in its surroundings computed with the approximation of a flow independent of the X_1-coordinate (Figure 2). The governing equations are first provided before presenting the 1-D numerical solution which reveals the spatial partitioning in deformation between simple shear and extension, first in the absence of the phase reaction and second, accounting for the phase transformation. A parametric study is finally presented to show the sensitivity of the localization process to the rheological and loading parameters.

3.1. Governing Equations

[23] The displacement field is constructed from the superposition of two modes of deformation and reads

$$\underline{u} = [u_s(X_2) + (\lambda_e - 1)X_1]\underline{e}_1 + \frac{\lambda_e - 1}{\lambda_e}X_2\underline{e}_2, \tag{8}$$

where $\{\underline{e}_i\}$ is the orthonormal basis. The second term of the horizontal component as well as the vertical component of the displacement are due to the stretch of the crust denoted λ_e and defined by $\lambda_e = 1 + \int_0^t V_e(t')\,dt'/L$ in which V_e is the imposed stretching velocity (Figure 2). Stretch results in a horizontal displacement contribution which is proportional to the horizontal position and defines the vertical displacement, which is also proportional to the vertical position. This vertical displacement ensures that the transformation is isochoric (no volume change). The second contribution $u_s(X_2)$ to the displacement field, which is the first contribution to the horizontal displacement in (8), is due to shear and is a function of the X_2-coordinate only.

[24] The transformation gradient $\underline{\underline{F}}$ (defined by $\underline{\underline{F}} = \underline{\underline{\delta}} + \nabla\underline{\underline{u}}$, where $\underline{\underline{\delta}}$ is the identity tensor and ∇ the gradient operator) is independent of the X_1-coordinate and reads

$$\underline{\underline{F}} = \begin{bmatrix} \lambda_e & u_{s,2} & 0 \\ 0 & \lambda_e^{-1} & 0 \\ 0 & 0 & 1 \end{bmatrix}. \tag{9}$$

Note again the superposition of the two modes of deformation and the fact that extension results in an homogeneous transformation. Consequently, strain localization can only be expressed through the distribution in displacement $u_s(X_2)$ and will thus be only along horizontal planes. The time derivative of the transformation gradient in (9) reads

$$\dot{\underline{\underline{F}}} = \begin{bmatrix} \dot{\lambda}_e & \dot{u}_{s,2} & 0 \\ 0 & -\dot{\lambda}_e\lambda_e^{-2} & 0 \\ 0 & 0 & 0 \end{bmatrix} \tag{10}$$

and is used to compute the Eulerian gradient of the velocity $\underline{\underline{L}} = \dot{\underline{\underline{F}}} \cdot \underline{\underline{F}}^{-1}$, which symmetric part is the rate of deformation tensor

$$\underline{\underline{D}} = \begin{bmatrix} \dot{\lambda}_e\lambda_e^{-1} & \frac{1}{2}\dot{\varepsilon}_s & 0 \\ \frac{1}{2}\dot{\varepsilon}_s & -\dot{\lambda}_e\lambda_e^{-1} & 0 \\ 0 & 0 & 0 \end{bmatrix}, \tag{11}$$

with $\dot{\varepsilon}_s = \dot{u}_{s,2}\lambda_e - \dot{\lambda}_e u_{s,2}$ and $\dot{\varepsilon}_s$ denoting the shear strain rate. Note that the incompressibility condition is satisfied since the trace of $\underline{\underline{D}}$ is zero. The equivalent strain rate for the combined extension and shear flow is defined in (3) and reads, for this 1-D problem

$$\dot{\varepsilon} = \sqrt{\dot{\varepsilon}_2^2 + \dot{\varepsilon}_s^2} \quad \text{with} \quad \dot{\varepsilon}_e = 2\dot{\lambda}_e/\lambda_e = 2V_e/(L\,\lambda_e), \tag{12}$$

in terms of the shear and the extension strain rate $\dot{\varepsilon}_e$.

[25] The deviatory part of the Kirchhoff stress tensor is proportional to the rate of deformation tensor according to (1) with a viscosity which is function of the history because of the potential phase transformation. The spherical part of the stress depends on the pressure p found from equilibrium. The first equation of equilibrium stipulates that the shear component of the stress ($\tau_{12} = \eta\dot{\varepsilon}_s$, equations (1) and (11)) is constant over the whole layer, while the second equilibrium equation is $\partial\tau_{22}/\partial X_2 - \rho g = 0$, with $\tau_{22} = -\eta\dot{\varepsilon}_e - p$. Integrating this second equation provides

$$p = p_{\text{litho}} - \eta\dot{\varepsilon}_e, \tag{13}$$

in terms of p_{litho}, the lithostatic equilibrium pressure in the current configuration. The lithostatic pressure is based on a volumetric mass distribution of 2700, 2800 and 3300 kg/m^3 in the upper crust, the lower crust and the mantle, respectively. Note that because of the viscosity, the pressure can be changed by up to 20% from its lithostatic value. This dependence explains why the extension strain rate controls the evolution of the pressure, and thus of the feldspar fracturing, and cannot exceed a certain range which will be established.

[26] To discuss the failure plane directions, we first introduce the principal stress direction defined by the angle α between the maximum principal stress and the horizontal axis (Figure 5) and is the ratio of the shear and extension strain rate:

$$\tan 2\alpha = \frac{2\tau_{12}}{\tau_{11} - \tau_{22}} = \frac{\dot{\varepsilon}_s}{\dot{\varepsilon}_e}. \tag{14}$$

In pure shear and simple shear, this angle is 90 and 45, respectively (Figures 5a and 5b). The orientation of potential shear failure in a band mode is related to α

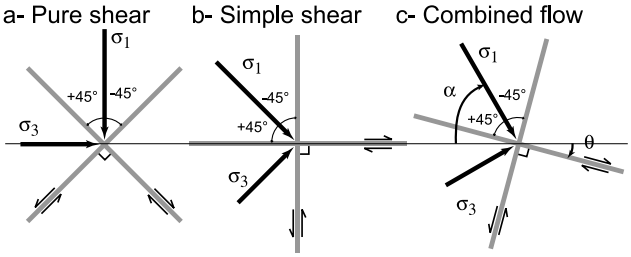

Figure 5. The orientation of the principal stresses and of the expected shear failure (a) in pure shear, (b) in simple shear, and (c) under combined flow.

assuming that the material is frictionless. Failure is then predicted at an angle θ that differs from α by ±45°, as shown in Figure 5. The band is at ±45° in pure shear and horizontal in simple shear. For combined modes of deformation, intermediate values are expected.

[27] The shear velocity v_s and the temperature T are the two unknowns and are a function of X_2 only. The solution of this 1-D problem is based on a finite-element approximation of the weak formulation of the equilibrium and the heat equations. Despite the addition of extension, the weak formulation is close to the one presented in paper 1 for simple shear and is not discussed further here. Readers are referred to *Gueydan* [2001] and *Gueydan et al.* [2001] for further information.

3.2. Partitioning of the Deformation in the Absence of Localization

[28] The strain rate and the orientation of potential shear failure are presented in Figure 6 for various velocity ratios V_e/V_s inhibiting the transformation (φ = 0, equation (6)) throughout the crust. The shear velocity V_s is set to the reference velocity V_R = 1.4 mm/a. These velocities are reached after a rise time t_L which has been studied in paper 1 for simple shear only. The depth of the reaction zone was then midcrustal (15 km) with t_L set to 1.4 ka. Shortening the rise time t_L leads to an increase in the applied constant shear stress, and thus to a transformation at greater depths. The same value of t_L (1.4 ka) is used in all simulations reported in this paper. The velocities are kept constant after t_L and results are obtained after a time lapse Δt of $3.10^2 t_L$ (420 ka), which is found sufficient for the reaction to be complete and the localization developed.

[29] For simple shear (V_e = 0), the strain rate $\dot{\varepsilon}$, shown as curve 0 in Figure 6a, increases exponentially with depth. The temperature sensitivity of the flow law (equation (6)), combined with the equilibrium condition of a constant shear stress over the lower crust, explain this trend. Note that the value of $\dot{\varepsilon}$ is of the order of $10^{-19} s^{-1}$ at the upper crust contact. This low value of the strain rate is a direct consequence of the low viscosity at the Moho. Mineralogical differences at that depth could alleviate that trend but was not considered in our analysis. It is proposed instead, and for sake of simplicity, to compare the equivalent strain rate for various velocity ratios with respect to this low value.

[30] A small amount of stretching ($V_e = 10^{-4} V_s$, curve 1, Figure 6a) induces an increase in strain rate at depths close to the upper crust contact. The stretching strain rate $\dot{\varepsilon}_e$ is constant over the lower crust and approximately equal to 2 V_e/L, if thinning is disregarded ($\lambda_e \sim 1$, equation (12)). Since at depths between 10 and

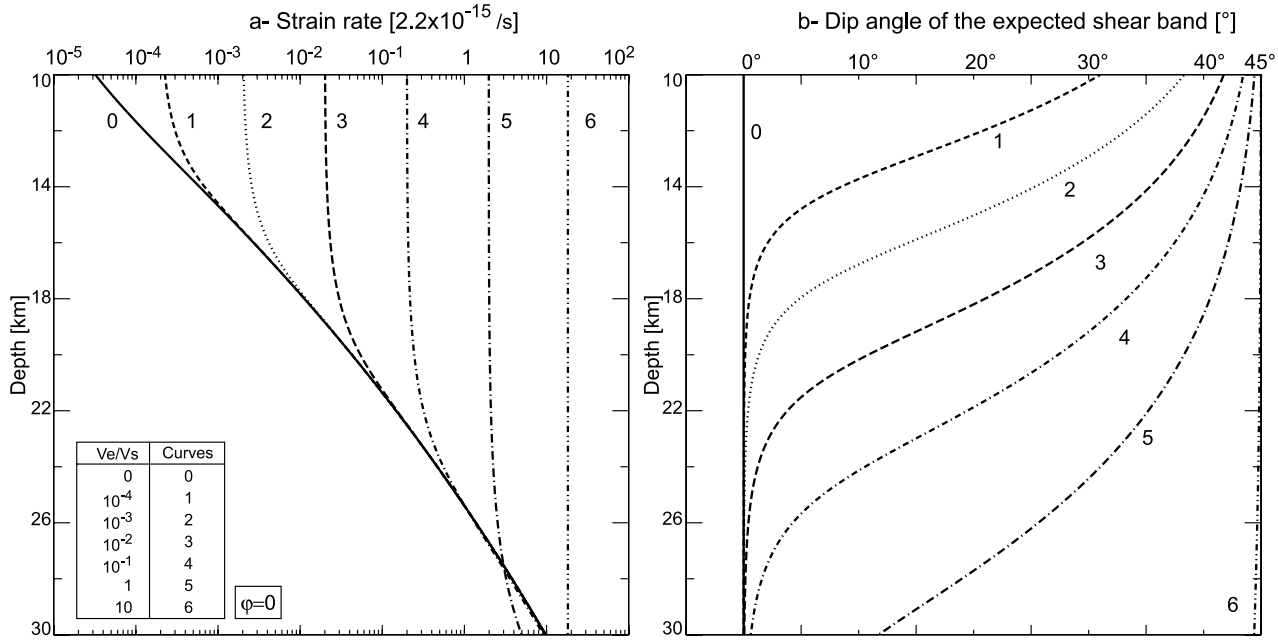

Figure 6. One-dimensional solution with transformation inhibited throughout the layer (φ = 0). The distribution of equivalent strain rate ($\dot{\varepsilon}$) and of the orientation of the expected shear bands is shown in Figures 6a and 6b, respectively, for different values of the velocity ratio V_e/V_s (between 0 and 10 for curves 0 to 6). The rise time t_L during which velocities are increased is set to 1.4 ka, and the velocities are kept constant thereafter. Observations are made after Δt of 420 ka.

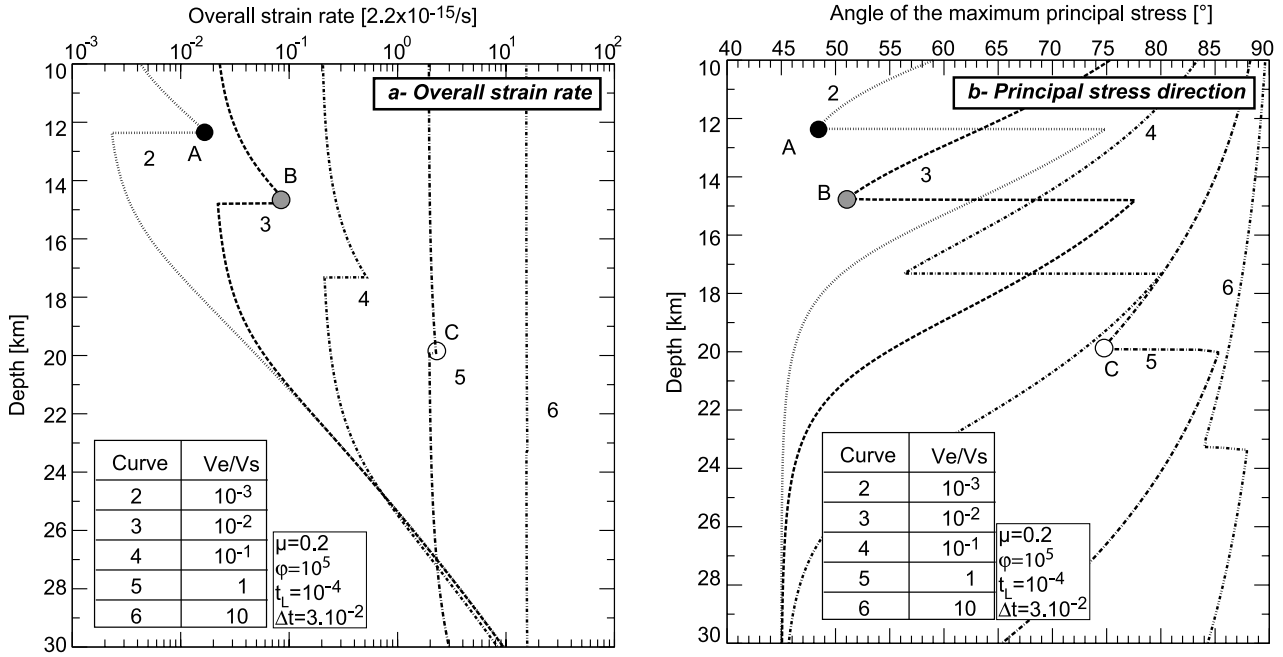

Figure 7. One-dimensional solutions with strain localization. The depth distribution of the equivalent strain rate ($\dot{\varepsilon}$) and the dip angle of the maximum principal stress σ_1 are shown in Figures 7a and 7b, respectively, for different values of the velocity ratio V_e/V_s. Note from the equivalent strain rate profiles and the orientation of the principal stress that the localization does not affect the lower crust below the reaction zone.

14 km, $\dot{\varepsilon}_s$ is less than $10^{-4}\dot{\varepsilon}_R$ (curve 0), an extension velocity as low as $10^{-4}V_R$ has a significant influence on the local strain rates, leading to a value of $\dot{\varepsilon} \simeq \dot{\varepsilon}_e$, and equal to $2.10^{-4}\dot{\varepsilon}_R$ (Figure 6a, curve 1). More generally, if $\dot{\varepsilon}_e$ is larger than $\dot{\varepsilon}_s$, the strain rate $\dot{\varepsilon}$ (equal to $\sqrt{\dot{\varepsilon}_e^2 + \dot{\varepsilon}_s^2}$, equation (12)) is then dominated by the stretching contribution ($\dot{\varepsilon} \sim \dot{\varepsilon}_e = 2\ V_e/L$) and remains constant over the whole layer as for curves 5 and 6. For ratios V_e/V_s varying from 0 to 0.1, the domain where the stretch controls the equivalent strain rate can be defined as the depth where the curves 1 to 4 are tangent to curve 0. This depth is thus increasing from 14 to 24 km, approximately.

[31] This partitioning between the upper part of the lower crust, where the stretching mode of deformation dominates ($\dot{\varepsilon} \simeq \dot{\varepsilon}_e$), and the lower part of the lower crust which essentially sustains simple shear ($\dot{\varepsilon} \simeq \dot{\varepsilon}_s$) is also reflected by the dip angle θ of the expected shear band in Figure 6b. This angle θ is computed from the principal stress orientation α, equation (14), as shown in Figure 5. For simple shear ($V_e = 0$, curve 0), the expected shear band is horizontal at all depths. For a velocity ratio of 10 (curve 6), the extension dominates over the whole structure and the expected shear bands are at ±45°. For intermediate depth, θ varies from 45° at shallow depth toward zero at Moho contact where simple shear dominates. Again, this rotation reflects the change with depth from the top region dominated by extension to the lower region dominated by simple shear.

[32] In summary, a combined flow between simple shear and extension leads to a partitioning of the mode of deformation. The midcrust is dominated by extension ($\dot{\varepsilon} = \dot{\varepsilon}_e$), whereas the deep crust mostly sustains simple shear ($\dot{\varepsilon} = \dot{\varepsilon}_s$). This is a direct consequence of the exponential decrease of the temperature-sensitive strength with depth.

3.3. Localization and Influence on the Principal Stress Orientation

[33] The strain rate profiles through the lower crust and the orientation of the principal stress are presented in Figure 7 for velocity ratios V_e/V_s between 10^{-3} and 10 (curves 2 to 6, same numbering as Figure 6) allowing for the feldspar-to-mica reaction to take place (with $\varphi = 10^5$ and $\mu = 0.2$). The new information for the equivalent strain rate profiles with localization is the existence of a jump in strain rate at depths varying between 12.2 km (curve 2, point A) and 20 km (curve 5, point C, Figure 7a). This jump marks the limit below which the transformation feldspar-mica is not activated because the Mohr-Coulomb criterion (equation (7)) is not satisfied. The larger the extension velocity V_e, the larger is the equivalent shear stress and the larger is the reduction in pressure (equation (13)), and thus the deeper can the reaction take place. Localization is found to occur within the reaction zone and share its lower limit. At shallower depths, the reaction has also been activated because the Mohr-Coulomb criterion is satisfied. The reaction is even completed there because no temperature sensitivity has been accounted for to control its progress. However, since the rheology is temperature sensitive, the strain rate decreases at shallower depths limiting the extend of the localization.

[34] The orientation α of the principal stress for these various choice in the velocity ratio V_e/V_s is plotted in Figure 7b according to equation (14). This angle reveals that there is a change in deformation mode in the reaction zone. Indeed the angle α decreases in the localization zone,

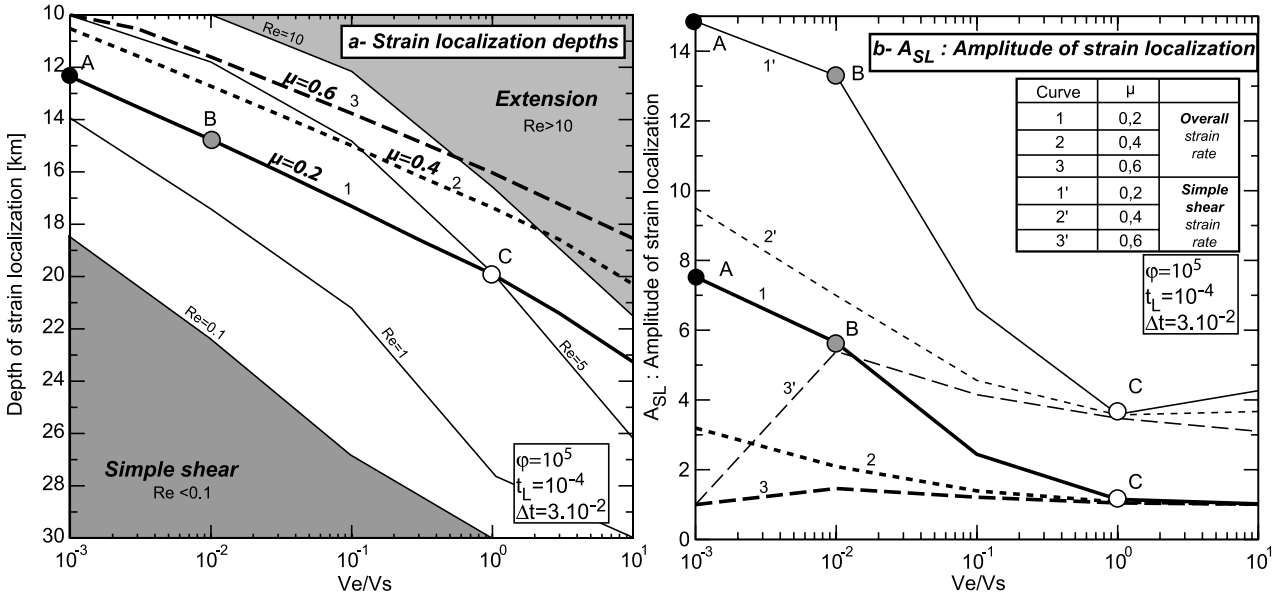

Figure 8. Parametric studies on the role of the velocity ratio V_e/V_s in setting (a) the depth of strain localization and (b) the amplitude of strain localization A_{SL}. In Figure 8a, R_e is the strain rate ratio $\dot{\varepsilon}_e/\dot{\varepsilon}_s$ prior to localization at a given depth. Regions where the deformation is primarily simple shear ($R_e < 0.1$) and extension ($R_e > 10$) are shaded. Note that the strain localization occurs in a region dominated by extension ($R_e > 1$). Points A, B, and C mark the position of the strain rate jump defined in Figure 7 for $\mu = 0.2$.

leading to an orientation consistent with a simple shear dominated flow. This trend is explained as follows. The orientation of σ_1 is dictated by the ratio $\dot{\varepsilon}_s/\dot{\varepsilon}_e$, equation (14). The extension strain rate being constant ($\dot{\varepsilon}_e \sim 2V_e/L$), the strain rate jump observed in the reaction zone is due to an increase of the shear strain rate $\dot{\varepsilon}_s$. The localization zone is thus marked by an increase of the strain rate ratio $\dot{\varepsilon}_s/\dot{\varepsilon}_e$, leading to a decrease of the principal stress angle.

[35] The intensity of the strain localization, defined by the jump in strain rate at the base of the reaction zone, decreases with increasing values of velocity ratio V_e/V_s, as shown by the strain rate profiles and the angle of σ_1 (Figure 7). For example, changing the ratio V_e/V_s from 10^{-3} (curve 2, point A) to 1 (curve 5, point C) leads to a reduction in the strain rate jump by a factor of four. Similarly, the decrease in the dip of the principal stress is larger for larger amplitude of the strain localization. More specifically, the localization zone is mostly dominated by simple shear flow for low values of V_e/V_s (point A, $\alpha \sim 45$) while stretching dominates within the entire lower crust for V_e/V_s of 1 (point C, $\alpha \sim 75$).

[36] This apparent contradiction that strain localization is less for large values of velocity ratio V_e/V_s is explained as follows. The localization direction θ (Figure 5) increases with larger V_e (equation (14)). Strain localization is thus less kinematically favorable with our 1-D assumption for larger V_e/V_s. This result is further explored in quantitative terms in the parametric study which follows.

3.4. Parametric Study of the Strain Localization

[37] The role of the velocity ratio V_e/V_s and of the reaction kinetics coefficient φ on the localization process are now discussed. This parametric study will be useful in explaining some of the 2-D results presented in the next section.

3.4.1. Role of the Velocity Ratio V_e/V_s

[38] The solid, dotted and dashed curves in Figure 8a, define the depth of the reaction zone - and thus the position of the jump in strain rate during strain localization - as a function of the velocity ratio V_e/V_s for the three values of the friction coefficient of 0.2, 0.4 and 0.6, respectively. Points A, B and C defined in Figure 7 have been also reported (curve 1, $\mu = 0.2$) for sake of completeness. These curves are approximately parallel and confirm that the depth of strain localization increases with the velocity ratio because of the associated increase in equivalent shear stress. On the same plot, the series of thin solid lines represent the ratio $R_e = \dot{\varepsilon}_e/\dot{\varepsilon}_s$ obtained in a simulation with no localization. The extension strain rate $\dot{\varepsilon}_e$ is set to the constant value of $\sim 2V_e/L$ for this computation, for sake of simplicity. The region where the deformation is almost only simple shear ($R_e < 0.1$) and almost pure extension ($R_e > 10$) are shaded. They correspond, as expected, to the lower and upper part of the lower crust, respectively. This series of thin lines is found useful to determine the mode of deformation which prevails at the onset of the strain localization. The interesting finding is that this mode is dominantly extension ($R_e > 1$) in the region crossed by the solid, dotted and dashed lines. The strain localization, which is in a shear mode, has thus to develop in an otherwise extensive regime. The quantitative assessment of this remark is done with Figure 8b.

[39] This figure presents the amplitude A_{SL} of the strain localization as a function of the velocity ratio V_e/V_s. Two definitions are proposed for that amplitude. The first, curves 1 to 3, corresponds to the ratio of overall strain rate $\dot{\varepsilon}$ in the presence and in the absence of strain localization at the same location. The second definition used for the series of curves $1'$ to $3'$ corresponds to the ratio of shear strain rate $\dot{\varepsilon}_s$ in the presence and in the absence of strain localization. For

each definition, three curves which are solid, dotted and dashed are proposed for the three values of the friction coefficient considered earlier (0.2, 0.4 and 0.6). To analyze this figure, consider first point A obtained for $V_e/V_s = 10^{-3}$ (Figures 8a and 8b) for which the localization is at the depth of 12 km and the strain rate ratio R_e prior to localization of the order of 2. The increase in simple shear strain rate due to strain localization is close to 15 (curve 1′, point A) and is therefore large enough to overprint the homogeneous extension strain rate and to induce an increase in overall strain rate by a factor of 8 (curve 1, point A). This development of the strain localization cannot take place for large values of the velocity ratio $V_e/V_s = 1$, as for example for point C. For that velocity ratio, the strain rate ratio R_e prior to localization at 19–20 km is 5 and the shear strain rate is increased by a factor of 4 only during localization (curve 1′, 2′ or 3′). This increase is not sufficient to overcome the dominant extension mode and therefore strain localization will not be expressed.

[40] The analysis of these two points can be generalized as follows. The strain localization dominates the flow if the ratio of extension strain rate over the shear strain rate is less than one. This ratio is simply R_e/A_{SL} in view of the definition given above for R_e and selecting the localization amplitude A_{SL} to be in terms of shear strain rates. For example, for $\mu = 0.6$, R_e is always larger than 5 for all the velocity ratio V_e/V_s (Figure 8a), the amplitude less than 5 (curve 3′, Figure 8b), and thus localization will not prevail. For $\mu = 0.4$ and for V_e/V_s less than 10^{-2} the amplitude A_{SL} is larger than 4 (curve 2′) and the ratio R_e of same magnitude, allowing strain localization to be expressed. Finally, for $\mu = 0.2$, the velocity ratio has to be less than 1 for the strain localization to manifest itself.

[41] In summary, localization will dominate the flow if the shear strain rate $\dot{\varepsilon}_s$ increases sufficiently so that the ratio R_e/A_{SL} is larger then one at the base of the reaction zone. This condition for localization is a direct consequence of our assumption of an homogeneous extensional mode of deformation which dominates within the upper part of the lower crust. This conclusion remains valid for the 2-D analysis presented next, since the extensional velocity V_e is introduced as boundary conditions. Since the friction coefficient is set to 0.2, the velocity ratio is chosen to be 10^{-3} for the 2-D analysis presented next, to obtain the maximum effect of the strain localization.

3.4.2. Role of the Feldspar-to-Mica Reaction Kinetics φ

[42] The amplitude of the strain rate increase in the shear zone is not only a function of the velocity ratio V_e/V_s, as discussed above, but also of the feldspar-to-mica reaction kinetics (Figure 9). The kinetics factor φ indeed controls the reaction time $t_R = 1/\varphi\dot{\varepsilon}$. Increasing either the strain rate or the reaction kinetics φ decreases the reaction time so that the reaction is completed faster and the strain localization develops faster. To explore this influence, we have plotted in Figure 9, the amplitude of the localization A_{SL} (based on the ratio of the overall strain rates) as a function of the velocity ratio for 3 values of the kinetic constant of 10^3, 10^4 and 10^5, corresponding to the dashed, dotted and solid curves, respectively.

[43] For a given velocity, the amplitude of the strain localization is less for smaller kinetic constant. At the time 420 ka ($\Delta t = 3.10^{-2}$) of the observation reported, the

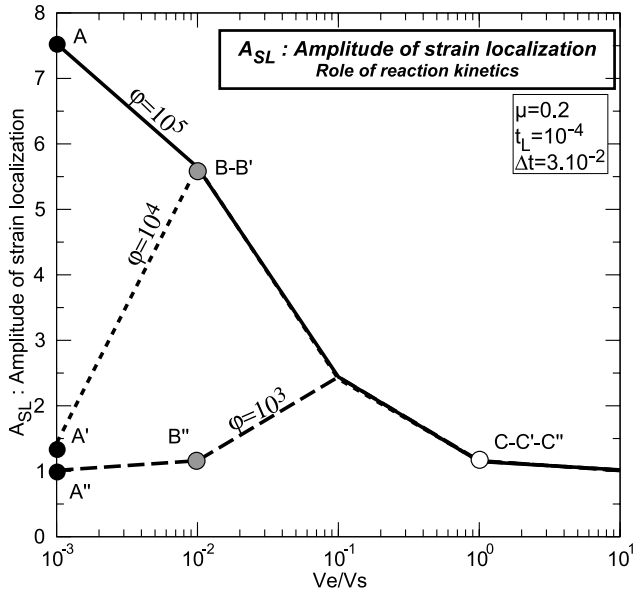

Figure 9. The influence of the feldspar-to-mica reaction kinetics φ on the amplitude of localization A_{SL}. Points A, B, and C of Figure 8 are reported and mark the position of the strain rate jump for $\mu = 0.2$ and $\varphi = 10^5$. Points (A′, B′, C′) and (A″, B″, C″ plotted for $\varphi = 10^4$ and $\varphi = 10^3$, respectively, have the same interpretation.

reaction is completed only for $\varphi = 10^5$ (point A), leading to a maximum increase of the strain rate in the shear zone. For smaller φ (point A′ and A″), the reaction time is greater, leading to partial feldspar-to-mica reaction. The amplitude of strain localization (Figure 9) is thus less important or even equal to 1 (e.g., no strain localization) for $\varphi = 10^3$ (point A″). This tendency is observed for larger values of the velocity ratio V_e/V_s. For example, for V_e/V_s larger than 0.1, the dashed, dotted and solid curves ($\varphi = 10^3$, 10^4 and 10^5, respectively) are identical. The localization is mild and the amplitude independent of the kinetic constant. This is explained by the increase in shear strain rate $\dot{\varepsilon}_s$ which is not sufficient to overcome the extension, a necessary condition for strain localization to prevail.

[44] Consequently, for the velocity ratio V_e/V_s of 10^{-3} and the friction coefficient $\mu = 0.2$, the kinetic constant φ has to be 10^5 to obtain the maximum strain rate increase within the shear zone. This value of φ determines the reaction time to be of the order of 4.10^{-3} (e.g., 56 ka) at the depth of localization. It was shown in paper 1 that this value of the reaction time leads to the formation of shear bands within half a million year. This formation lapse is short compared to the time of exhumation (less than 10 Ma) in metamorphic core complexes [*Gautier and Brun*, 1994; *Lister and Davis*, 1989; *Jolivet et al.*, 1998]. However, the exhumation time referred first to the formation and activity (e.g., large displacement along the shear zone) of midcrustal shear zone and second, to the final stage of unroofing in the upper brittle crust. The formation of the midcrustal shear zone should thus be short compared to the exhumation time. It is for this reason that a fast reaction kinetics (φ of 10^5) was proposed in paper 1, again to be consistent with relatively fast exhumation in core complexes, and is kept for the 2-D simulations to be presented.

[45] In summary, the value of the velocity ratio V_e/V_s of 10^{-3} leads to the largest strain rate increase at depth of 12.2 km, using a friction coefficient for feldspar fracturing of $\mu = 0.2$ and $\varphi = 10^5$. This set of parameters has thus been selected for the 2-D analysis presented next. From this 1-D analysis, it can be concluded that an increase of the velocity ratio V_e/V_s will have at least three consequences for the strain localization process: first a decrease of the amplitude of strain localization, second an increase of the depth of strain localization and third an increase of the dip angle of the shear zone. This third conclusion is partly contradicted by the findings of the 2-D analysis, as it will be seen in the next section.

4. Two-Dimensional Solution for Combined Shear and Extension

[46] The geometry of the studied structure and the boundary conditions are given in Figure 2 with the loading conditions identical to the one considered for the 1-D analysis. The initial conditions are the 1-D simple-shear steady states discussed above. The overall evolution of the structure is first presented before discussing the details of the stress distribution in the reaction zone.

4.1. Midcrustal Flat Weakened Zone and Local Failure Criterion

[47] The distribution over the 2-D domain of the equivalent strain rate and of the secant viscosity is presented in the form of colored isocontours in Figure 10 obtained after various time lapses Δt ranging from 0 (end of rise time) to 420 ka. The results are presented in a window of the domain between the depths of 10 and 17 km and over the 20 km length of the structure. The range of isocontours covers one order of magnitude in both strain rate and viscosity.

[48] The 2-D solution at the end of the rise time ($\Delta t = 0$) exhibits a variation along the first coordinate axis X_1 because of boundary effects at the four corners of the periodic domain (Figure 2b). The simple shear velocity V_s imposed at the two top corners leads to a local stress field which is not consistent with equilibrium for the initially horizontal and stress-free boundary at the top. As a consequence, the top layer (upper crust) rotates to relax these stresses and to satisfy equilibrium. The wavelength of the wavy pattern observed in Figure 10 at $\Delta t = 0$ is thus controlled by the length of the cell studied. At that time, the average value of the strain rate at a given depth is very close to the distribution observed in one dimension (curve 2, Figure 7).

[49] After a Δt of 14 ka, the strain rate and viscosity distributions show a slight discontinuity at the depth of approximately 12.5 km. That depth is the lower limit of the reaction zone below which the feldspar fracturing does not take place. Feldspar-to-mica reaction initiates at the base of the reaction zone which is almost horizontal because the Mohr-Coulomb criterion is pressure sensitive. The reaction zone, which is the region where feldspar-to-mica reaction has been activated, is therefore almost flat. The slight variation of the depth of feldspar fracturing, below the yellow lenticular region in strain rate and viscosity profiles, is explained by the variation of pressure induced by the wavy pattern discussed above. At this time, the mica concentration has already changed from 10 to 18% in the lenticular region where the strain rate is already multiplied by a factor of five.

[50] After Δt = 70 ka, the region of high strain rate (yellow color) and low viscosity (blue color) is the region where the feldspar-to-mica reaction has mostly progressed. The largest mica concentration is already 0.4 there. The lowest mica concentration at the same depth is 0.25. At this time, the lenticular region of larger strain rate terminates to the right in a 27° right-hand-side dipping shear band. This dip angle corresponds to the orientation of the failure band predicted in the 1-D analysis (curve 2, Figure 7b). The stress concentration ahead of that propagating shear band leads to the activation of the Mohr-Coulomb criterion below the initial depth of reaction. Also, the stress concentration leads to the minor activation of a left-hand-side dipping conjugate shear band. Note that this secondary feature propagates upward and enter a zone of higher viscosity and gets reflected further to the right, initiating a second shear band, dipping toward the shearing direction. The intersection of that second shear band with the lower limit of the reaction zone is another site for stress concentration. The same phenomenon is observed on the left-hand side of the lenticular region of the strain rate plot.

[51] This pattern of conjugate shear bands reflecting and propagating to the right and left continues to develop as can be observed from time 140 to 420 ka. At that later time, the primary shear bands dominate and the conjugates are less visible because of an unloading on both sides of the major bands. Right-hand side dipping shear bands dominate because of the top-to-the-right shearing imposed on the structure (Figure 2). The development of low dipping shear bands at that time becomes more uniform along the reaction zone because the reaction is completed in the region where it was first initiated. Indeed, after 140 ka, the reaction is completed only in the main low dipping shear band (mica concentration of 0.50) which is marked by the low (dark blue) viscosity.

[52] The bands do not propagate deeper because the stress concentration ahead of the shear bands is not sufficient to trigger the Mohr-Coulomb criterion which is necessary for the onset of the reaction. The completion of the reaction within the bands marks the end of the destabilizing effect and thus of the band thinning typical of localization. The band thinning is essential in promoting the stress concentration as expected in geometrically singular regions.

[53] These 2-D numerical results are partly mesh-size dependent: a decrease in the mesh size results in finer shear bands with an influence on the horizontal length between two adjacent shear bands within the flat weakened zone. However, the mathematical problem treated is not ill-posed since the end of the phase reaction terminate the destabilizing role of the rheology and sets a minimum size to the shear bands. Furthermore, the mesh size is already sufficiently small to ensure that the dip angle of shear bands and, to a lesser degree, that the amplitude of strain localization are well captured. Consequently, the mechanical properties of the flat weakened zone discussed next will not be modified by further mesh-size reduction.

[54] In summary, the main finding of this 2-D analysis is that the initial lower limit of the feldspar-to-mica reaction

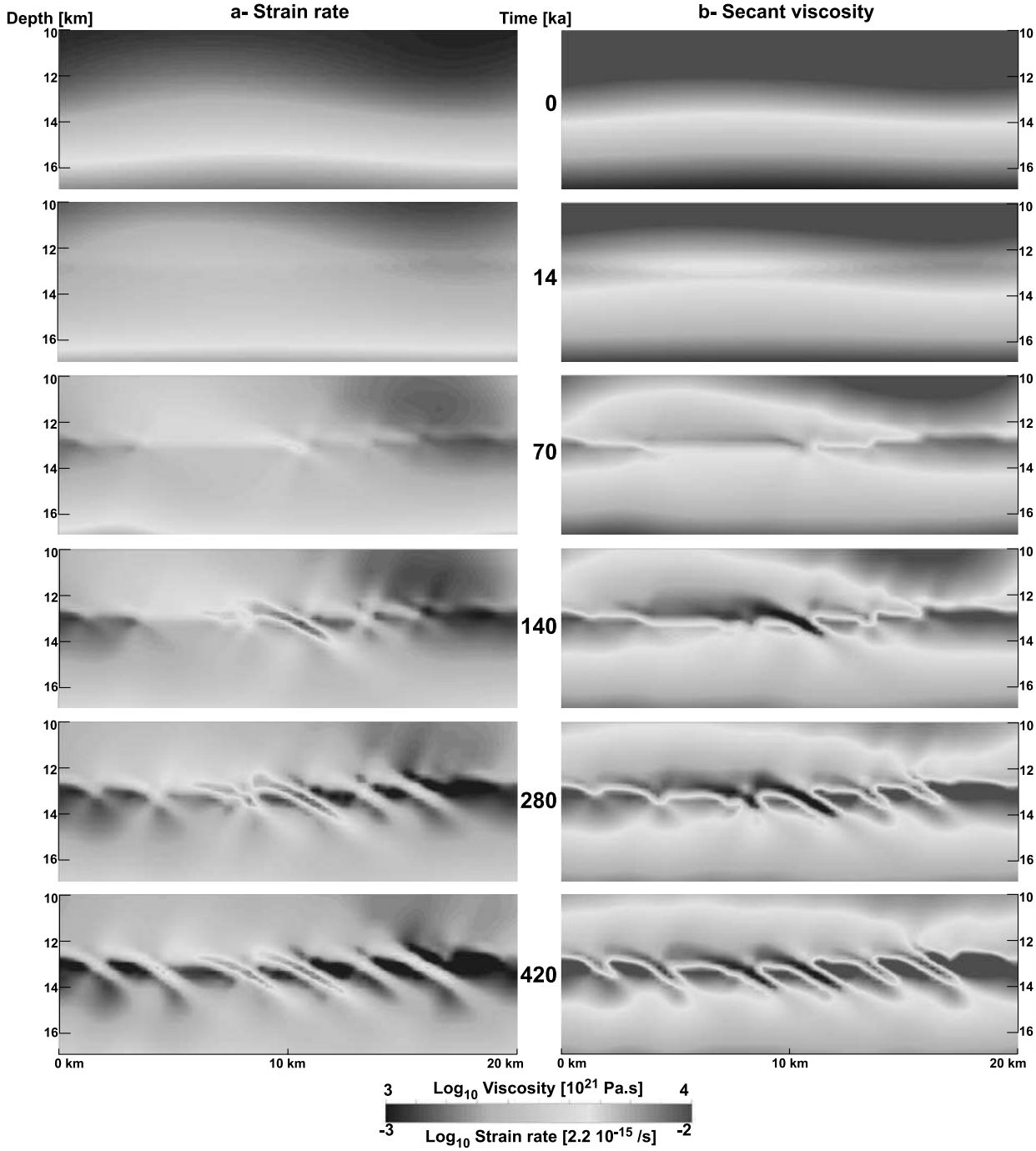

Figure 10. Equivalent strain rate (left column) and viscosity (right column) isocontours at the midcrust at different time Δt after the end of the velocity changes. See color version of this figure at back of this issue.

zone is horizontal, irrespective of the velocity ratio, and corresponds to the feldspar brittle-ductile transition. In this region, the conditions for localization are met and shear band orientation is governed by the local stress field, which is sensitive to the velocity ratio V_e/V_s. A periodic system of approximately 30° dipping shear bands has developed after less than half a million years and defines a flat weakened zone at midcrustal depth. This flat zone is weak in the sense that the viscosity is reduced, due to strain localization. Its internal structure, and especially the dip angle of the shear bands, is a marker of the mixity in deformation mode.

4.2. Stress Analysis Within the Midcrustal Flat Weakened Zone

[55] The stress state within the flat weakened zone formed at midcrustal depths is now examined in details. The information presented on Figure 11 are extracted from the central region of the subdomain presented in Figure 10, and corresponds to a window of 9 × 6 km at time Δt = 280 ka.

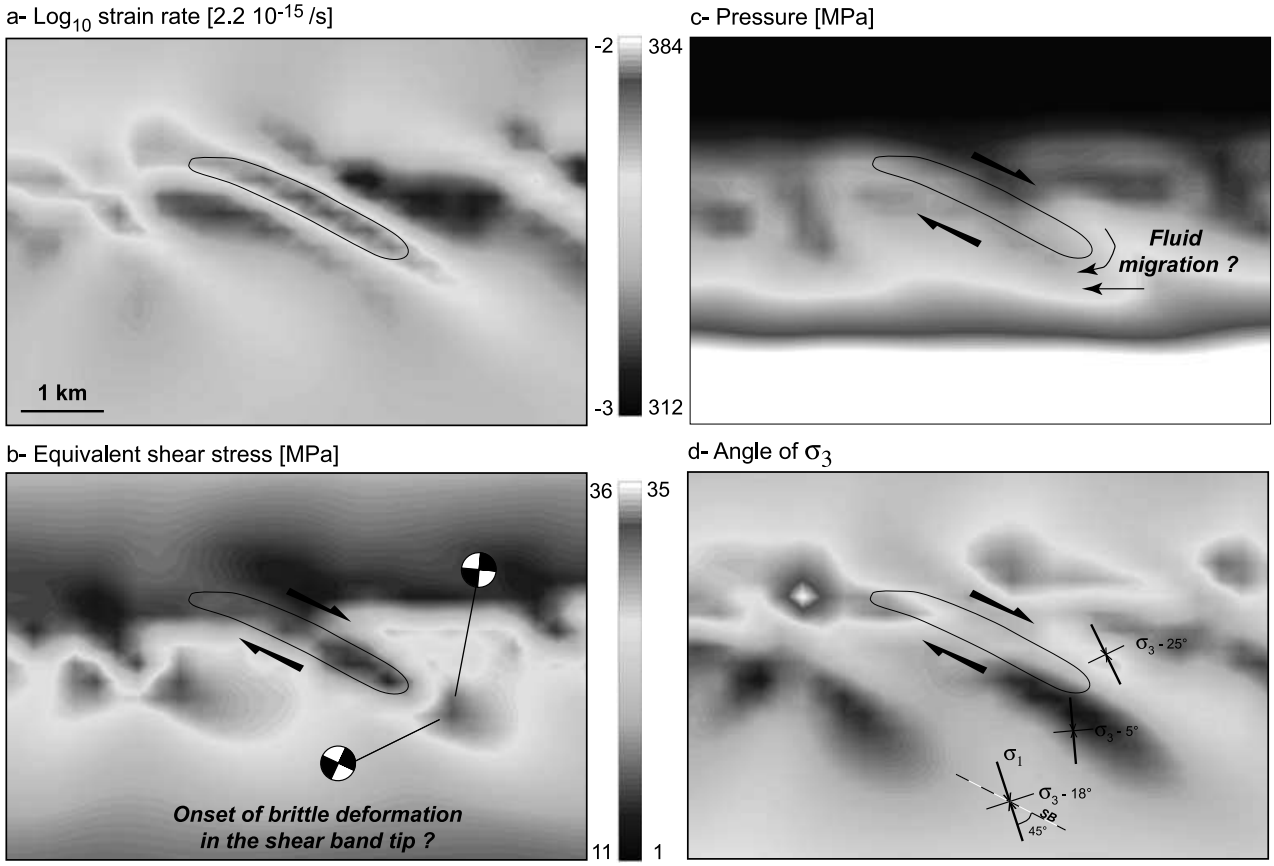

Figure 11. The equivalent strain rate, stress, pressure, and the orientation of the minor principal stress in the form of isocontours over the region which is central to Figure 10 at time 280 ka. See color version of this figure at back of this issue.

[56] Figure 11a shows the central shear band in terms of isocontours of strain rates. The two dark blue regions mark the unloading that takes place outside the shear band, which is typical of strain localization. The core of the band is outlined by a solid curve to facilitate its positioning in other plots of the same figure. The fact that the core of the band, as well as the upper part of the reaction zone, is weakened is seen in Figure 11b, where isocontours of the equivalent shear stress are plotted. Note the stress concentration (a factor of three) ahead of the band where the material has not transformed. Similar stress concentrations are seen ahead of the band to the left. There is a third stress concentration below that second shear band due to the activation of a conjugate minor shear band that is better seen from the strain rate isocontours in Figure 11a. Figure 11c presents isocontours of the pressure which is larger on the right-hand side of the main band than on the left-side. This observation is consistent with the dextral sense of shear during localization. To facilitate the interpretation of these results, we have also plotted in Figure 11d, the distribution in orientation of the minor principal stress σ_3. The minor stress orientation is defined to obtain a smooth distribution between 0° and 45°. Note the rapid rotation of the stress field around the tip of the main shear band, from 5° to 25°. Again, this rotation of the stress field around the band is a direct consequence of the dextral sense of shear during localization.

[57] The stress concentration at the shear band tips and the pressure gradient, of the order of 50 MPa, in the vicinity of the shear bands are now tentatively used to shed light on potential seismogenic activity and fluid migration at the brittle-ductile transition of the continental crust.

5. Discussion

[58] There are two consequences of the complex internal structure of the brittle-ductile transition which can be explained in terms of the stress state just presented. First, the large local shear stress ahead of the band tips could lead to the activation of brittle deformations. Focal mechanisms presented in Figure 11b are constructed assuming that the orientation of the failure plane is at 30° of the major principal stress σ_1, which corresponds to a frictional solid with an internal friction angle of 30°. The orientation varies over a short distance because of the rotation of the principal stresses around the shear band (Figure 11d). Brittle deformation mechanisms, not accounted for in our simulations, could facilitate the propagation of the reaction zone downward and also contribute to the shear band anastomosis within the weakened zone. The shear stress concentration at the band tips could also lead to the triggering of microearthquakes. These earthquakes should be localized in the flat weakened domain at midcrustal depth, with low dip angle nodal plane (Figure 11b). This mechanism could

therefore explain the presence of microseismic clusters located at depth ranging between 6 and 11 km below region of active extension, as in the Gulf of Corinth [*Rigo et al.*, 1996; *Rietbrock et al.*, 1996]. Moreover, in continental rift regions with high extension rates (extensional velocity larger than 1 cm/a), several recent observations indicate that large earthquakes ($M_w \sim 6.0$) can occur on low dipping normal faults, mostly in the Woodlark Rift and in the Aegean Rifts [*Abers*, 2001]. Those active low-angle normal faults are subparallel to extensional shear zones found in the metamorphic core complexes. This observation, which questioned the failure mechanics within the brittle crust, could be tentatively explained with our simulations as follows. Again, the account of brittle deformation should facilitate the anastomosis of ductile shear bands within the weakened zone, defining a flat or low-angle weak fault. This fault, which nucleate subparallel to the preexisting shear zones, could explain the formation of flat-lying detachment faults and, consequently, the associated seismicity. The mechanical feasibility of such brittle anastomosis of ductile shear bands remains however to be constrained and is the objective of future work.

[59] The second consequence of these numerical simulations comes from the analysis of the pressure distribution, presented in Figure 11c. The pressure gradient of the order of 50 MPa at the tip of the shear band over a length of less than one kilometer must result in the migration of fluids, if present at that depth. Fluid migration toward the footwall of the band should enhance the progress of the reaction and therefore thicken the band. Such fluid migration could partly explain the formation of a large number of quartz-rich veins in the vicinity of the shear zones, as observed in the field [*Patriat and Jolivet*, 1998; *Roller et al.*, 2001]. In the Woodlark Basin detachment fault zone, it has been indeed proposed that the abundance of mineralized veins in the mylonites suggests that deformation was not entirely ductile, but includes embrittlement [*Roller et al.*, 2001]. Our results could therefore explain the embrittlement at the shear band tip, leading to the formation of veins which are oriented parallel to the foliation. Fluid migration generated by the observed pressure gradient could also induce a change in the thermal regime, from a purely conductive regime to an advective one, leading to a rapid cooling along the shear zones, as recently imaged by $\delta^{18}O$ analysis by *Famin* [2003].

[60] The comparison of our predictions with field data collected in exhumed fossil shear zones is certainly difficult. The sense of shear, the dip angle and the P-T conditions are similar to those observed in Alpine Corsica, in the Tyrrhenian Sea or in the Aegean [*Jolivet et al.*, 1998]. However, the structure seen today in the field is the result of a much longer evolution ($\sim$10 Ma) than the one presented here. The long term evolution of these shear bands remains unknown. One interpretation is that finite amounts of extension and simple shear would inevitably lead to the exhumation of the ductile crust and to the concentration of shearing along one major shear zone which connects to the upper crust. Capturing this long term evolution by numerical means is certainly a challenge for future research. A further limitation is the chosen mineralogy. The rheological model was designed to reproduce the lithology observed along the East Tenda Shear Zone in Alpine Corsica where a monzogranite is progressively deformed and transformed into a mica-rich mylonite [*Daniel et al.*, 1996]. In the Cyclades, very different lithologies are leading to similar structural evolution: the collapsed Hellenic belt shows a mixture of metapelites, metabasites and marbles in which the extensional shear zones develop [*Lister et al.*, 1984; *Jolivet and Patriat*, 1999], excepted where late granitoïds have intruded the crust [*Faure et al.*, 1991; *Lee and Lister*, 1992]. Other destabilizing factors should be proposed to explain localization in such lithologies where the phyllosilicates are already a major component before the formation of the shear zones.

[61] A word on the geological relevance of the velocity ratios necessary for strain localization is now required. In regions of active extension, GPS horizontal velocities are typically 1 cm/a. The surface horizontal velocity used in our simulations is either V_s or $V_s + V_e$, as shown in Figure 2. Since ductile strain localization is triggered only for low values of the velocity ratio, the surface velocity is approximately V_s. It is of the order of 1 mm/a in our modeling mainly because of the limited validity of our rheological model at the depth of the Moho. Further development, for example accounting for the grain-size sensitivity, should permit velocities comparable to the GPS measures. One can already states, however, that low angle extensional shear zones nucleate only if extension is mostly accommodated by shearing and not stretching at depth. This conclusion of our simulations is consistent with the following geological observations made in metamorphic core complexes. In the Tyrrhenian and the Aegean Seas, extensional shear zones at the brittle-ductile transition and major normal faults show a constant polarity on several hundreds of kilometers (top-to-the-east in the Tyrrhenian Sea, top-to-the-north in the Aegean Sea) suggesting a significant component of simple shear [*Jolivet et al.*, 1994, 1998]. The origin of this dominant shearing flow within the lower crust remains however a matter of debate. Three main causes are commonly evoked to explain this trend. First, the fracturing in the upper crust leads to the rigid gliding of the upper crust over the lower crust (Figure 1) [*Lister and Davis*, 1989]. Second, the presence of lower crustal flow, which is only likely to occur in prethickened continental crust, will induce a simple shearing within the lower crust [*McKenzie et al.*, 2000]. Third, at much larger scale, when slab roll-back is active, extension will take place in the back-arc region, where a strong basal shearing could occur at the base of the lithosphere, due to the trench suction [*Jolivet et al.*, 1998]. This basal shearing, which is enhanced by the slab roll-back, would also promote simple shearing. The relative importance of each processes and their geological relevance are of course of great interest but were definitely beyond the scope of this paper.

6. Conclusion

[62] The aim of this paper was first to study the initial development of low-angle extensional shear zones at the brittle-ductile transition due to strain localization and, second, to understand their orientation which contradicts classical failure criterion. The rheological model used accounts for reaction-softening (feldspar-to-mica reaction), activated by feldspar fracturing, a condition detected by the

Mohr Coulomb criterion [*Gueydan et al.*, 2003]. The 2-D numerical solutions shows the development of a flat weakened zone at midcrustal depths (12–14 km). It is the pressure-sensitivity of the feldspar grain failure criterion which controls the horizontal orientation of the weakened zone. This zone is weak because the reaction has soften the material (reduction of the viscosity by one order of magnitude). Its internal structure is defined by periodic extensional shear bands, dipping at 30° toward the shearing direction, an orientation which is consistent with the predictions of local failure criterion. The shear stress is found at the tip of the shear bands to be enhanced by a factor of at least three. This stress concentration could explain the embrittlement of the midcrust, responsible for the onset of microearthquakes with low dip angle nodal planes [*Rigo et al.*, 1996] and the formation of numerous veins, as it is observed in the field [*Patriat and Jolivet*, 1998; *Roller et al.*, 2001].

[63] The proposed mechanical model has thus some merit but should be amended in the future to clarify at least the two following points. First, the feldspar-to-mica reaction is not relevant for all midcrustal shear zones formed during postorogenic extension. In the Cyclades [*Lister et al.*, 1984; *Jolivet and Patriat*, 1999] and in the Basin and Range [*Davis*, 1983; *Miller et al.*, 1983; *Lister and Davis*, 1989; *Wernicke*, 1992], very different lithologies (metapelites, metabasites and marbles) are leading to the development of low dipping extensional shear zones. Other destabilizing factors should thus be proposed to explain localization in such lithologies. Second, brittle deformation mechanisms has been inferred from the results of our simulations but were not introduced in the rheology, except to detect feldspar fracturing. An important step forward in the modeling of the continental crust under extension will be the simultaneous account of the brittle faulting in the upper crust and the ductile strain localization in the lower crust. Brittle deformation should also facilitate the downward and lateral propagation of the reaction and ultimately leads to the anastomosis of shear bands within the weakened zone, defining a flat or low-angle weak normal fault.

[64] **Acknowledgments.** The authors would like to thank Denis Gapais for useful comments on a first version of the manuscript. The reviews of Ian Main, Jean Chéry, and the Associate Editor Isabelle Manighetti helped us in preparing the final version of this paper.

References

Abers, G. A. (1991), Possible seismogenic shallow-dipping normal faults in the Woodlark-d'Entrecasteaux extensional province, Papua New Guinea, *Geology*, *19*, 1205–1210.

Abers, G. A. (2001), Evidence for seismogenic normal faults at shallow dips in continental rifts, in *Non-volcanic Rifting of Continental Margins: A Comparison of Evidence From Land and Sea*, edited by R. C. L. Wilson et al., pp. 305–318, Geol. Soc. Spec. Publ.

Abers, G. A., C. Z. Mutter, and J. Fang (1997), Earthquakes and normal faults in the Woodlark-d'Entrecasteaux rift system, Papua New Guinea, *J. Geophys. Res.*, *102*, 15,301–15,317.

Anderson, E. M. (1951), *The Dynamics of Faulting*, 206 pp., Oliver and Boyd, White Plains, N. Y.

Avigad, D., G. Baer, and A. Heimann (1998), Block rotations and continental extension in the Central Aegean Sea: Paleomagnetic and structural evidence from Tinos and Mykonos, *Earth Planet. Sci. Lett.*, *157*, 23–40.

Braun, J., J. Chéry, A. Poliakov, D. Mainprice, A. Vauchez, A. Tomassi, and M. Daignières (1999), A simple parametrization of strain localization in the ductile regime due to grain size reduction: A case study for olivine, *J. Geophys. Res.*, *104*(B11), 25,167–25,181.

Buck, W. R. (1988), Flexural rotation of normal faults, *Tectonics*, *7*(5), 959–973.

Burchfiel, B. C., K. V. Hodges, and L. H. Royden (1987), Geology of Panamint Valley-Saline Valley pull-apart system, California: Palinspastic evidence for low-angle geometry of a Neogene range-bounding fault, *J. Geophys. Res.*, *92*, 10,422–10,426.

Daniel, J. M., L. Jolivet, B. Goffé, and C. Poinssot (1996), Crustal-scale strain partitioning: Footwall deformation below the Alpine Corsica Oligo-Miocene detachement, *J. Struct. Geol.*, *18*, 41–59.

Davis, G. H. (1983), Shear-zone model for the origin of metamorphic core complexes, *Geology*, *11*, 342–347.

de Bresser, J. H. P., J. H. Ter Heege, and C. J. Spiers (2001), Grain size reduction by dynamic recrystallization: Can it result in major rheological weakening?, *Int. J. Earth Sci.*, *90*, 28–45.

Dixon, J., and G. Williams (1983), Reaction softening in mylonites from the Arnaboll thrust, Sutherland, *Scott. J. Geol.*, *19*(2), 157–168.

Famin, V. (2003), Incursion de fluides dans une zone de cisaillement ductile (Tinos, Cyclades, Grece): Mecanismes de circulation et implications tectoniques, doctoral thesis, Univ. Pierre et Marie Curie, Paris.

Faure, M., M. Bonneau, and J. Pons (1991), Ductile deformation and syntectonic granite emplacement during the late Miocene extension of the Aegean (Greece), *Bull. Soc. Geol. Fr.*, *162*, 3–12.

Fitz Gerald, J. D., and H. Stünitz (1993), Deformation of granitoids at low metamorphic grade. I: Reactions and grain size reduction, *Tectonophysics*, *221*, 269–297.

Fleitout, L., and C. Froidevaux (1980), Thermal and mechanical evolution of shear zones, *J. Struct. Geol.*, *2*(1/2), 159–164.

Gautier, P., and J. P. Brun (1994), Crustal-scale geometry and kinematics of late-orogenic extension in the central Aegean (Cyclades and Evvia island), *Tectonophysics*, *238*, 399–424.

Gueydan, F. (2001), La transition fragile-ductile de la croûte continentale en extension. Du terrain à la modélisation, doctoral thesis, Univ. Pierre et Marie Curie, Paris.

Gueydan, F., Y. M. Leroy, and L. Jolivet (2001), Grain size sensitive flow and shear stress enhancement at the brittle-ductile transition of the continental crust, *Int. J. Earth Sci.*, *90*(1), 181–196.

Gueydan, F., Y. M. Leroy, L. Jolivet, and P. Agard (2003), Analysis of continental midcrustal strain localization induced by microfracturing and reaction-softening, *J. Geophys. Res.*, *108*(B2), 2064, doi:10.1029/2001JB000611.

Jackson, J. A. (1987), Active normal faulting and continental extension, *Geol. Soc. Spec. Publ.*, *28*, 3–18.

Jolivet, L., and M. Patriat (1999), Ductile extension and the formation of the Aegean Sea, in *The Mediterranean Basins: Tertiary Extension Within the Alpine Orogen*, edited by B. Durand et al., *Geol. Soc. Spec. Publ.*, *156*, 427–456.

Jolivet, L., J. P. Brun, P. Gautier, S. Lallemant, and M. Patriat (1994), 3-D kinematics of extension in the Aegean from the Early Miocene to the Present, insight from the ductile crust, *Bull. Soc. Geol. Fr.*, *165*, 195–209.

Jolivet, L., C. Faccenna, B. Goffé, M. Mattei, F. Rossetti, C. Brunet, F. Storti, R. Funiciello, J. P. Cadet, and T. Parra (1998), Mid-crustal shear zones in post-orogenic extension: The northern Tyrrhenian Sea case, *J. Geophys. Res.*, *103*(B6), 12,123–12,160.

King, G., Z. Ouyang, P. Papadimitriou, A. Deschamps, A. Gagnepain, G. Houseman, J. Jackson, C. Soufleris, and J. Virieux (1985), The evolution of the Gulf of Corinth (Greece): An aftershock study of the 1981 earthquake, *Geophys. J. R. Astron. Soc.*, *80*, 677–693.

Koch, P. S., J. C. Christie, A. Ord, and J. R. P. George (1989), Effect of water on the rheology of experimentally deformed quartzite, *J. Geophys. Res.*, *94*(B10), 13,975–13,996.

Kronenberg, A. K., S. H. Kirby, and J. Pinkston (1990), Basal slip and mechanical anisotropy of biotite, *J. Geophys. Res.*, *95*(B12), 19,257–19,278.

Laigle, M., A. Hirn, M. Sachpazi, and N. Roussos (2000), North Aegean crustal deformation: An active fault imaged to 10 km depth by reflection seismic data, *Geology*, *28*(1), 71–74.

Lee, J., and G. S. Lister (1992), Late Miocene ductile extension and detachment faulting, Mykonos, Greece, *Geology*, *20*, 121–124.

Lister, G. S., and G. A. Davis (1989), The origin of metamorphic core complexes and detachment faults formed during Tertiary continental extension in the northern Colorado River region, U.S.A., *J. Struct. Geol.*, *11*(1/2), 65–94.

Lister, G. S., G. Banga, and A. Feenstra (1984), Metamorphic core complexes of cordilleran type in the Cyclades, Aegean Sea, Greece, *Geology*, *12*, 221–225.

Mandl, G. (1988), *Mechanics of Tectonic Faulting*, 407 pp., Elsevier Sci., New York.

McKenzie, D., F. Nimmo, J. A. Jackson, P. B. Gans, and E. L. Miller (2000), Characteristics and consequences of flow in the lower crust, *J. Geophys. Res.*, *105*(B5), 11,029–11,046.

Melosh, H. J. (1990), Mechanical basis for low-angle normal faulting in the Basin and Range province, *Nature*, *343*, 331–335.

Miller, E. L., P. B. Gans, and J. Garling (1983), The Snake river decollement: An exumed mid-Tertiary brittle-ductile transition, *Tectonics*, *2*, 239–263.

Mitra, G. (1978), Ductile deformation zones and mylonites: The mechanical process involved in the deformation of crystalline basement rocks, *Am. J. Sci.*, *278*, 1057–1084.

Ord, A., and B. E. Hobbs (1989), The strength of the continental crust, detachment zones and the development of plastic instabilities, *Tectonophysics*, *158*, 269–289.

Patriat, M., and L. Jolivet (1998), Post-orogenic extension and shallow-dipping shear zones, study of a brecciated decollement horizon in Tinos (Cyclades, Greece), *C. R. Acad. Sci., Ser. IIa*, *326*, 355–362.

Poirier, J. P. (1980), Shear localization and shear instability in materials in the ductile field, *J. Struct. Geol.*, *2*(1/2), 135–142.

Rietbrock, A., C. Tibéri, F. Scherbaum, and H. Lyon-Caen (1996), Seismic slip on a low-angle normal fault in the Gulf of Corinth: Evidence from high resolution cluster analysis of microearthquakes, *Geophys. Res. Lett.*, *23*(14), 1817–1820.

Rigo, A., H. Lyon-Caen, R. Armijo, A. Deschamps, D. Hatzfeld, K. Makropoulos, P. Papadimitriou, and I. Kassaras (1996), A microseismicity study in the western part of the Gulf of Corinth (Greece): Implications for large-scale normal faulting mechanisms, *Geophys. J. Int.*, *126*, 663–688.

Roller, S., J. H. Behrmann, and A. Kopf (2001), Deformation fabrics of faulted rocks, and some syntectonics stress estimates from the active Woodlark Basin detachment zone, in *Non-volcanic Rifting of Continental Margins: A Comparison of Evidence From Land and Sea*, edited by R. C. L. Wilson et al., *Geol. Soc. Spec. Publ.*, *187*, 319–334.

Rutter, E. H., and K. H. Brodie (1988), The role of tectonic grain size reduction in the rheological stratification of the lithosphere, *Geol. Rundsch.*, *77*(1), 295–308.

Shelton, G., and J. Tullis (1981), Experimental flow laws for crustal rocks, *Eos Trans. AGU*, *62*(17), 396.

Simpson, C. (1985), Deformation of granitic rocks across the brittle-ductile transition, *J. Struct. Geol.*, *7*(5), 503–511.

Sorel, D. (2000), A Pleistocene and still-active detachment fault and the origin of the Corinth-Patras rift, Greece, *Geology*, *28*, 83–86.

Structural Analysis and Rock Physics Program (2003), LMS, Ecole Polytech., Palaiseau, France.

Wernicke, B. (1981), Low-angle normal faults in the Basin and Range province: Nappe tectonics in an extending orogen, *Nature*, *291*, 645–648.

Wernicke, B. (1992), Cenozoic extensional tectonics of the U.S. cordillera, in *The Cordilleran Orogen: Conterminous U.S.*, edited by B. C. Burchfiel, P. W. Lipman, and M. L. Zoback, pp. 553–581, Geol. Soc. of Am., Boulder, Colo.

Wernicke, B. (1995), Low-angle normal faults and seismicity: A review, *J. Geophys. Res.*, *100*(B10), 20,159–20,174.

Wernicke, B. P., and G. J. Axen (1988), On the role of isostasy in the evolution of normal fault systems, *Geology*, *16*, 848–851.

Westaway, R. (1999), The mechanical feasibility of low-angle normal faulting, *Tectonophysics*, *308*, 407–443.

White, S. H., and R. J. Knipe (1978), Transformation- and reaction-enhanced ductility in rocks, *J. Geol. Soc. London*, *135*, 513–516.

Wibberley, C. A. J. (1999), Are feldspar-to-mica reactions necessarily reaction-softening processes in fault zones?, *J. Struct. Geol.*, *21*, 1219–1227.

F. Gueydan, Géosciences Rennes, Université de Rennes 1, UMR CNRS 6118, 35042 Rennes Cedex, France. (frederic.gueydan@univ-rennes1.fr)

L. Jolivet, Laboratoire de Tectonique, Université Pierre et Marie Curie, UMR CNRS 7072, T26-0E1, Case 129, 4 place Jussieu, 75252 Paris Cedex 05, France. (laurent.jolivet@lgs.jussieu.fr)

Y. M. Leroy, Laboratoire de Mécanique des Solides, Ecole Polytechnique, UMR CNRS 7649, 91128 Palaiseau Cedex, France. (leroyy@lms.polytechnique.fr)

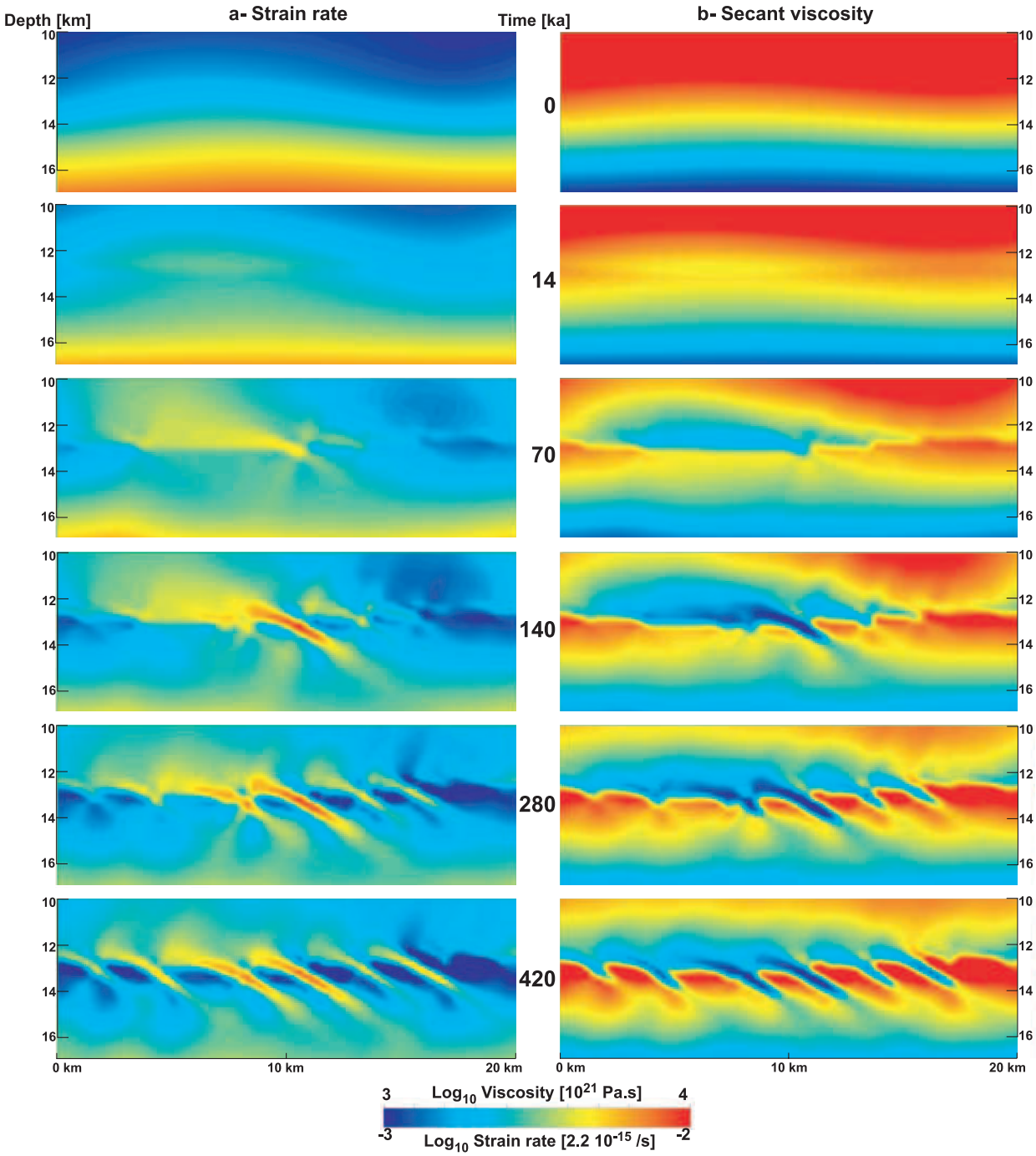

Figure 10. Equivalent strain rate (left column) and viscosity (right column) isocontours at the midcrust at different time Δt after the end of the velocity changes.

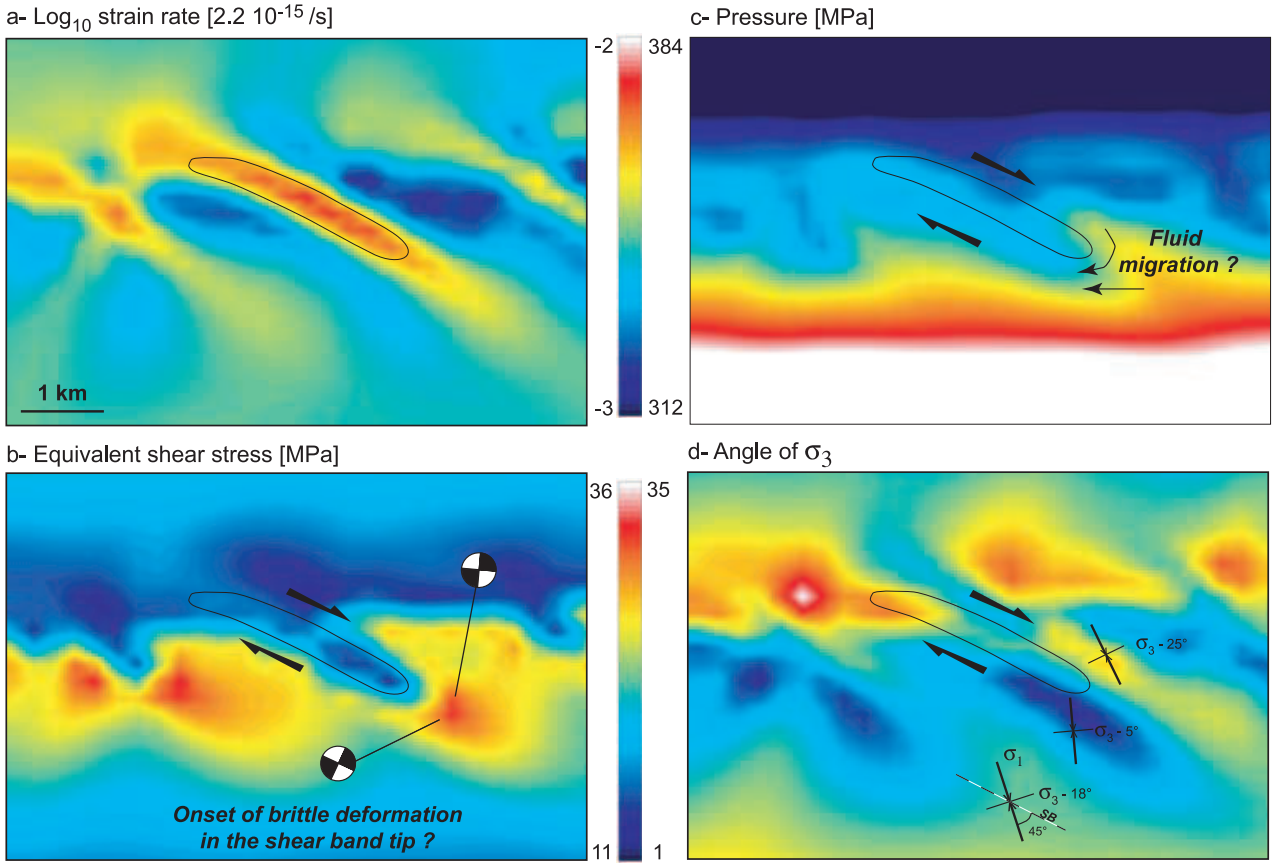

Figure 11. The equivalent strain rate, stress, pressure, and the orientation of the minor principal stress in the form of isocontours over the region which is central to Figure 10 at time 280 ka.